Check-probe spectroscopy of lifetime-limited emitters in bulk-grown silicon carbide

van de Stolpe, G. L.; Feije, L. J.; Loenen, S. J.H.; Das, A.; Timmer, G. M.; de Jong, T. W.; Taminiau, T. H.

DOI
10.1038/s41534-025-00985-3

Publication date
2025

Document Version
Final published version

Published in
NPJ Quantum Information

npj | quantum information

Article

Published in partnership with The University of New South Wales

https://doi.org/10.1038/s41534-025-00985-3

Check-probe spectroscopy of lifetime-limited emitters in bulk-grown silicon carbide

G. L. van de Stolpe[1,2,3], L. J. Feije[1,2,3], S. J. H. Loenen[1,2,3], A. Das[1,2], G. M. Timmer[1,2], T. W. de Jong[1,2] & T. H. Taminiau[1,2] ✉

Solid-state single-photon emitters provide a versatile platform for exploring quantum technologies such as optically connected quantum networks. A key challenge is to ensure the optical coherence and spectral stability of the emitters. Here, we introduce a high-bandwidth 'check-probe' scheme to quantitatively measure (laser-induced) spectral diffusion and ionisation rates, as well as homogeneous linewidths. We demonstrate these methods on single V2 centres in commercially available bulk-grown 4H-silicon carbide. Despite observing significant spectral diffusion under laser illumination ($\gtrsim$GHz s^{-1}), the optical transitions are narrow (~35 MHz), and remain stable in the dark ($\gtrsim$1 s). Through Landau-Zener-Stückelberg interferometry, we determine the optical coherence to be near-lifetime limited (T_2 = 16.4(4) ns), hinting at the potential for using bulk-grown materials for developing quantum technologies. These results advance our understanding of spectral diffusion of quantum emitters in semiconductor materials, and may have applications for studying charge dynamics across other platforms.

Optically active solid-state defects have enabled pioneering experiments in the field of distributed quantum computation[1–4] and quantum networks[5,6]. Proof-of-principle experiments have demonstrated primitives for quantum error correction[1–3] and the realisation of a three-node network[7,8]. Key to these applications is the ability to connect multiple emitters via their coherent spin-optical interface, with many applications requiring narrow, stable optical transitions[6,7].

Spectral diffusion of the transitions, caused by fluctuating charge impurities within the bulk material or at the surface, poses a major challenge, especially when emitters are integrated in nanostructures[9–12]. Moreover, laser pulses used to probe or manipulate the emitter can exacerbate such diffusion[10,13]. Experimental techniques that enable the quantitative study of spectral diffusion and its timescales provide insight into the environmental charge dynamics, potentially allow for targeted optimisation of material properties and fabrication processes, and enable pathways to mitigate diffusion through pre-selection[13,14]. However, commonly used methods may significantly disturb the system through continuous laser illumination, complicating the unambiguous determination of transition line widths and diffusion rates under different laser illumination conditions[9,10,15–17].

Here, we introduce a comprehensive check-probe spectroscopy toolbox for characterising and mitigating spectral diffusion of single solid-state emitters. Our methods offer high-bandwidth, quantitatively extract diffusion and ionisation rates, and introduce minimal system disturbance from laser illumination, enabling accurate measurements even in heavily diffusive environments. Additionally, our work provides a framework for the quantitative analysis of heralded preparation of the charge environment, which has become an indispensable tool to mitigate spectral diffusion in quantum network and other experiments[3,7,8,13,14,18].

We apply these methods to study single k-site V_{Si} (V2) centres (a next-generation candidate for quantum networks[15,19,20]), embedded in nanopillars etched in commercially available bulk-grown 4H-silicon carbide (SiC)[21,22]. This system exhibits a high degree of spectral diffusion (>1 GHz diffusion-averaged linewidth), typical for single quantum emitters in bulk-grown silicon or silicon carbide[23,24]. First, we determine spectral diffusion rates with and without laser illumination. Using this knowledge, we select configurations of the system with narrow spectral transitions, which can be tuned over the breadth of the inhomogeneous linewidth and can be stored for over a second and accessed on-demand. Finally, through the observation of Landau-Zener-Stückelberg interference[25], we determine the optical coherence time to be: T_2 = 16.4(4) ns, consistent with the lifetime limit for these defects[26].

Although high-purity epitaxial layers provide a starting point with less spectral diffusion[15,19,27] (Supplementary note 8), our observation of lifetime-limited coherence in nanostructures in bulk-grown silicon

[1]QuTech, Delft University of Technology, Delft, The Netherlands. [2]Kavli Institute of Nanoscience Delft, Delft University of Technology, Delft, The Netherlands. [3]These authors contributed equally: G. L. van de Stolpe, L. J. Feije, S. J. H. Loenen. ✉e-mail: t.h.taminiau@tudelft.nl

carbide, hints towards the possibility of using such mass-fabricated material for quantum technology development and applications. Furthermore, the techniques developed here might facilitate the targeted optimisation of material and fabrication recipes, and can be readily transferred to other platforms[18,24,28–30].

Results

Single V2 centres in bulk-grown silicon carbide

We consider spectral diffusion caused by fluctuating charges in the environment of the emitter, for example, associated with material impurities or surface defects that modify the optical transition frequency via the Stark shift[31–34]. Although these dynamics are largely frozen at cryogenic temperatures[17], charges can still be mobilised through laser illumination used for the optical addressing of the emitter[9,10,17,24] (Fig. 1a). In particular, charges can be excited to the conduction (or valence) band via a single-photon process if the energy difference from the occupied charge state is smaller than the associated energy of the laser frequency (Fig. 1b). Subsequent decay to a different spatial position causes fluctuations in the electric field at the location of the emitter[10,17].

Although our methodology applies to a range of emitter types, materials, and operating temperatures, this work specifically considers single k-site V_{Si} (V2) centres in commercially available bulk-grown silicon carbide at 4K. In this material, diffusion is likely caused by charges associated with residual defects and shallow dopants (concentrations ~10^{15} cm^{-3}) that are created during the growth process[35]. We apply two types of lasers: a 785 nm 'repump' laser for charge-state reinitialisation (~10 μW), and two frequency-tunable near-infrared ('NIR') lasers (~10 nW) for resonant excitation of the V2 centre's spin-dependent A_1 and A_2 zero-phonon-line transitions (Fig. 1b and d)[19].

We fabricate nanopillars that enhance the optical collection efficiency (Methods), to mitigate the effects of the unfavourable dipole orientation in c-plane 4H-SiC (Fig. 1c). In about one in every 10 pillars, we observe a low-temperature spectrum with a characteristic zero-phonon line at 916 nm (Fig. 1d), hinting at the presence of single V2 centres confined to the nanopillars. The dimensions of the nanopillar, with a diameter of ~500 nm and a height of ~1.2 μm, mean that surface- and fabrication-related effects might contribute to the diffusion dynamics.

Photoluminescence excitation spectroscopy

First, we measure the V2 diffusion-averaged optical absorption linewidth via photoluminescence excitation spectroscopy (PLE). By repeatedly interleaving repump pulses ('R', 10 μs, 10 μW) with NIR pulses at a varying frequency f_1 (10 μs, 10 nW, Fig. 1e), we randomise the V2 charge environment before each repetition, effectively averaging over many spectral configurations. In a system without spectral diffusion, we would expect to observe two distinct narrow lines (FHWM of ~26 MHz and ~11 MHz), separated by $\Delta \approx 1$ GHz[19,26,36], corresponding to the separation of the A_1 and A_2 transitions. However, we observe a broad Gaussian peak (2.4(1) GHz, see Fig. 1f), hinting at a high degree of spectral diffusion, consistent with comparable experiments in similar bulk semiconductor materials[24,28].

In order to probe the individual A_1 and A_2 transitions, we employ a two-laser PLE scan[28]. Compared to the sequence in Fig. 1e, we now fix frequency f_1 close to the middle of the broad resonance (Fig. 1f) and add a second NIR laser at frequency f_2 (Fig. 2a). We observe a significant increase in the detected count rate when the frequency difference satisfies: $f_2 - f_1 \approx \Delta = 954(2)$ MHz, explained by a strong reduction in optical pumping (which otherwise quickly diminishes the signal[28]). Importantly, the relatively narrow resonance condition (FWHM of 89(9) MHz) observed in Fig. 2b

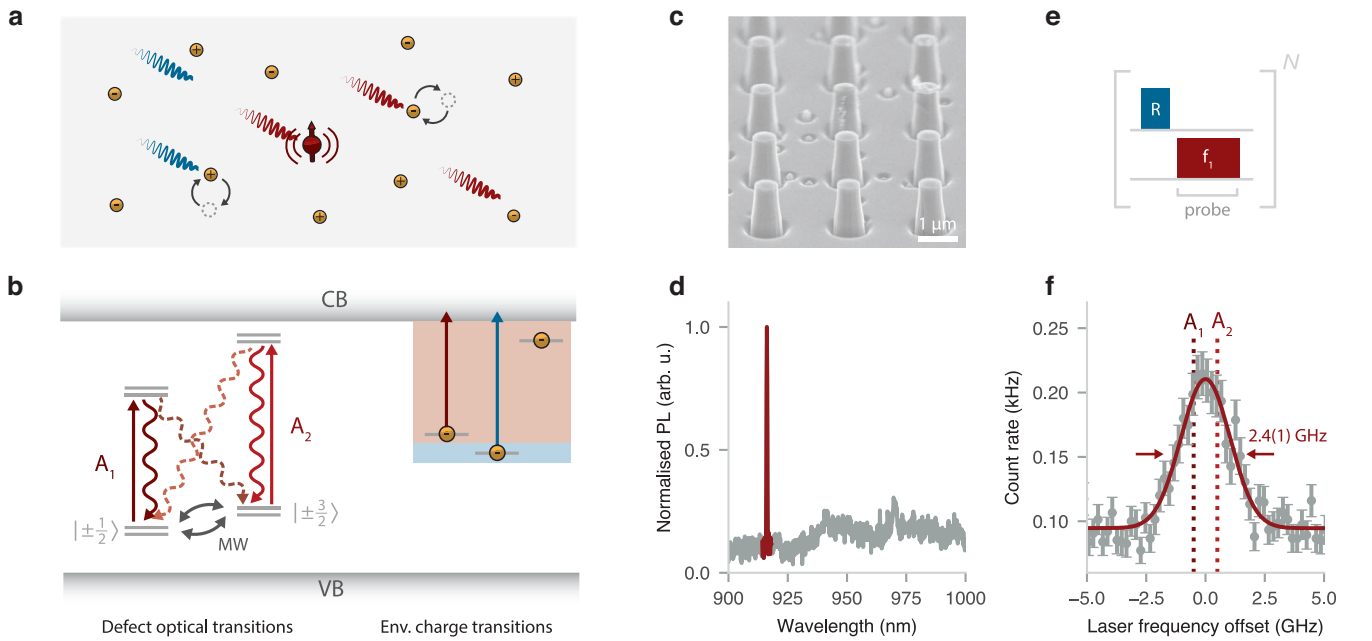

Fig. 1 | Emitter optical properties and laser-induced charge dynamics. **a** Schematic of the system. A single V2 centre in SiC is surrounded by charges (yellow circles) associated to intrinsic residual impurities[35]. Under laser illumination, these charges can be mobilised after excitation to (from) the conduction (valence) band, indicated by blue and red wiggly lines. **b** Energy diagram, depicting the V2 centre's optical transitions (left) and possible laser-induced charge dynamics of the (unknown) impurities in the environment (right). The spin-dependent A_1 and A_2 transitions can be excited with a tunable, near-infrared (NIR) laser (916 nm, red arrow), while a high-energy repump laser (785 nm, blue arrow) is used to scramble the charge state of the V2 centre and its environment. The ground-state spin ($S = \frac{3}{2}$) can be manipulated with microwave (MW) radiation. **c** Scanning-electron-microscopy image of a sample used in this work, which is diced from a 4 inch commercially available 4H-SiC bulk wafer. Nanopillars (~500 nm diameter) are fabricated to improve the photon collection efficiency. **d** Representative low-temperature (4K) emission spectrum of a V2 centre under repump-laser excitation, showing the characteristic zero-phonon line at 916 nm (red highlight). **e** Experimental sequence of the diffusion-averaged photoluminescence-excitation spectroscopy (PLE). The frequency f_1 of the NIR laser (red) is scanned over the V2 zero-phonon line, while emission in the phonon sideband is collected. The repump laser (blue) scrambles the charge state of the emitter and its environment before every repetition (total N). **f** Measured PLE spectrum. Averaging over many charge-environment configurations results in a single, broad peak (2.4(1) GHz FWHM) that encompasses the A_1 and A_2 transitions (separated by ~1 GHz). The laser frequency is offset from 327.10 THz.

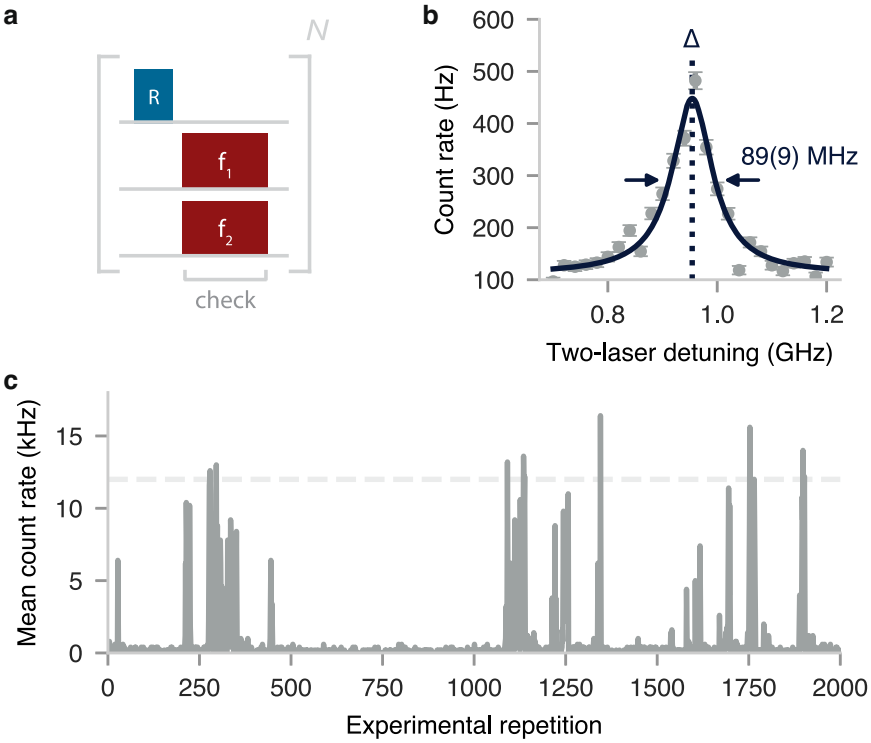

Fig. 2 | Two-laser photoluminescence excitation spectroscopy. a Experimental sequence. A short (10 μs, 10 μW) high-energy (785 nm) repump laser pulse ('R') partially scrambles the charge state of both the environment and the V2 centre. Emission is collected during the 'check' block, when two NIR lasers at frequencies f_1 and f_2 are turned on (approximately resonant with the broad peak in Fig. 1g). **b** We observe an increase in count rate if the laser frequency difference is equal to Δ = 954(2) MHz, the spacing between the A_1 and A_2 transitions. A Lorentzian fit obtains an FWHM of 89(9) MHz. **c** Detected mean count rate per experimental repetition, when the length of the 'check' block is set to 5 ms. In most repetitions, the defect is off-resonant with the lasers. When the A_1 and A_2 transitions coincide with laser frequencies f_1 and f_2, we observe significant emission ($\gg$1 kHz). Thresholding (dashed line) on the detected counts can be employed to prepare specific (i.e. 'on resonance') spectral configurations of the V2 centre.

suggests that the homogeneous linewidth is much narrower than the diffusion-averaged linewidth in Fig. 1f.

Next, we fix the laser frequency difference to Δ and record the counts per experimental repetition (Fig. 2c). We obtain a telegraph-like signal, consistent with a single V2 centre that is spectrally diffusing. Such a signal allows for the implementation of a charge-resonance check[14,18], which probes whether the V2 centre is in the desired negative charge state, and its two transitions are resonant with the NIR lasers. If the number of detected counts passes a threshold T (e.g. the grey dashed line in Fig. 2c), we conclude that the defect was on resonance in that specific experimental repetition, allowing for post-selection (or pre-selection) of the data. In the following, we will explore how such post-selection tactics can be exploited to gain insights in the spectral diffusion dynamics.

Check-probe spectroscopy: ionisation and diffusion dynamics

Next, we develop a method to measure the ionisation and spectral diffusion dynamics of the V2 centre. Currently, various experimental techniques exist, based either on tracking the transition frequency with subsequent PLE scans[10,15,16], or on autocorrelation-type measurements[9,37]. The former method struggles with measuring dynamics faster than the acquisition timescale of a single scan[15,38] (yielding ~Hz bandwidth typically, see also Supplementary Fig. 8). The latter, although fast (up to ~GHz bandwidth), offers limited flexibility for probing diffusion under external perturbations[9].

Here, we take a different approach, based on a pulsed *check-probe* scheme as outlined in Fig. 3a. Following a charge-randomization (repump) step, two 'check' blocks are executed (as in Fig. 2a), separated by a perturbation of the system (grey block marked 'X'). Such a perturbation might consist of turning on (or off) specific lasers (e.g. NIR or repump) during the delay time t. This pulsed scheme allows for the isolation of diffusion originating from the perturbation from other sources with a high bandwidth. The timescales for the perturbation are only limited by the modulation speed and timing resolution of the laser pulses and perturbation, providing potential bandwidths in the gigahertz regime (e.g. using electro-optic modulation).

Importantly, one can either post-select on high counts (i.e. 'check') in the block before, or after the perturbation, effectively initialising the emitter on resonance at the start, or at the end of the experiment. By 'probing' the emitter brightness after (before) the perturbation, we effectively track its evolution forward (backward) in time, denoted as delay time $t > 0$ ($t < 0$) in Fig. 3a. This allows for the distinction between time-symmetric and non-time-symmetric perturbation processes (e.g. spectral diffusion or ionisation of the emitter, see Fig. 3b), as opposed to evaluating the purely symmetric autocorrelation function[9].

To quantitatively describe the signal, we derive an analytical expression that takes into account spectral diffusion and ionisation of the emitter. In this system, spectral diffusion is mainly caused by laser-induced reorientation of charges surrounding the defect, whose dynamics can be approximated by a bath of fluctuating electric dipoles[17]. To model this, we employ the spectral propagator formalism[38,39], which describes the evolution of the spectral probability density function in time, and whose form is given by a Lorentzian with linearly increasing linewidth $\gamma(t) = \gamma_d\,|t|$[39] (with γ_d the effective diffusion rate). Note that this description is valid only at short timescales ($\gamma_d\,|t| \ll 1$ GHz), as the spectral probability density should eventually converge to the diffusion-averaged distribution observed in Fig. 1f[39]. Furthermore, we take the spectral propagator to be time-symmetric, and model the ionisation (charge recapture) of the emitter as an exponential decay of fluorescence, governed by rate γ_i (γ_r).

The mean number of observed counts at delay time t can be described by (Supplementary note 1):

$$C(t) = \begin{cases} C_0\left(1+\gamma_d t/\Gamma\right)^{-1} e^{-\gamma_i t}, & \text{if } t>0 \\ C_0\left(1-\gamma_d t/\Gamma\right)^{-1} e^{\gamma_r t}, & \text{otherwise}. \end{cases} \quad (1)$$

with C_0 the mean number of observed counts at $t = 0$, Γ the emitter's (Lorentzian) homogeneous linewidth, and γ_d, γ_i, $\gamma_r > 0$. Note that Eq. (1) in general does not obey time-inversion symmetry (for $\gamma_i \neq \gamma_r$), and in specific cases allows for a clear distinction between ionisation and diffusion processes (e.g. if $\gamma_r \approx 0$, see Fig. 3b). Next to that, the functional form of Eq. (1) captures information about the type of processes at play: emitter charge dynamics are described by an exponential decay while spectral diffusion has a power law dependence.

We experimentally implement the sequence for three distinct perturbations: (i) no laser illumination (Fig. 3c), (ii) illumination with the two NIR

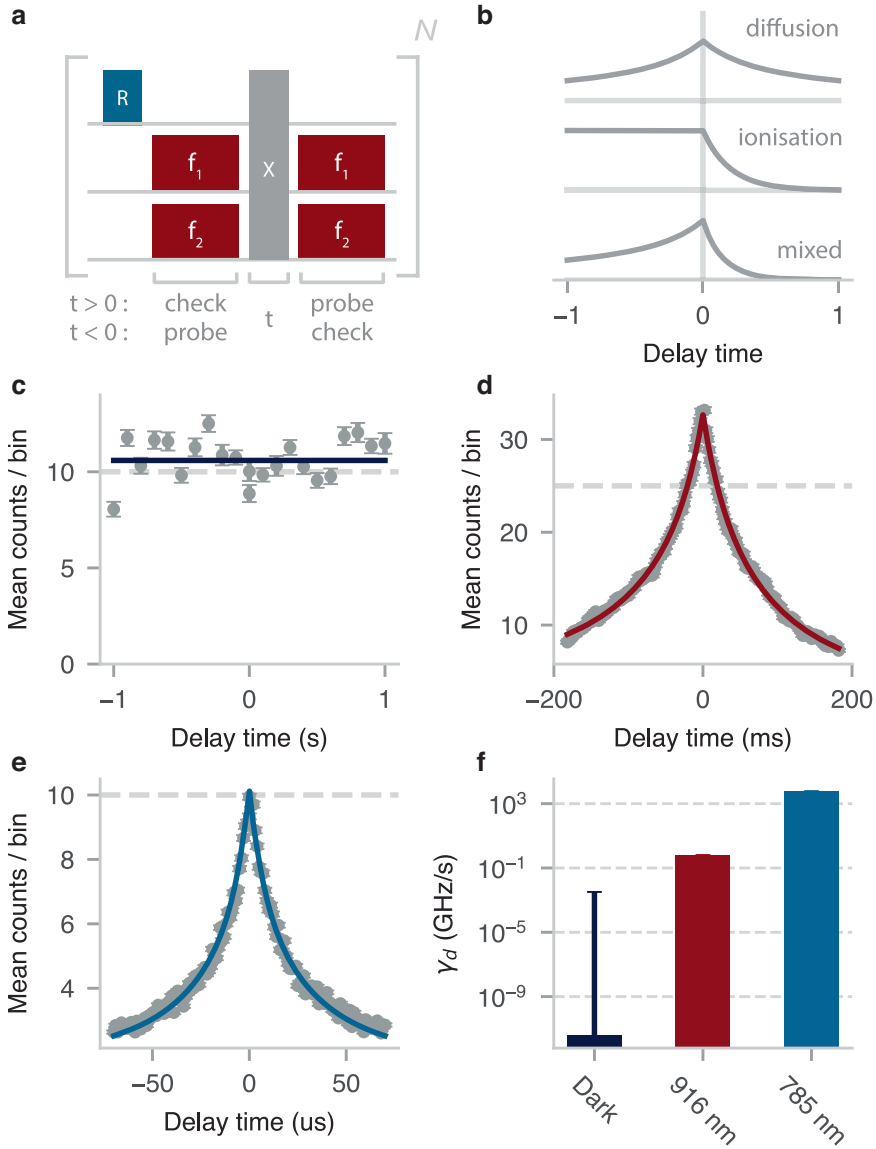

Fig. 3 | Spectral diffusion dynamics. **a** Experimental sequence. A 'check' block (2 ms, 20 nW) is followed by a system perturbation (marked 'X'), which here consists either of turning off the lasers (**c**), turning on the NIR lasers (**d**), or turning on the repump laser (**e**). A second block (2 ms, 20 nW) probes whether the defect has diffused away, or has ionised (denoted 'probe'). Data is post-selected by imposing a minimum-counts threshold (T), heralding the emitter on resonance in the first (second) block and computing the mean number of counts in the second (first) block, which encodes the emitter brightness at future (past) delay times t. **b** Schematic illustrating the expected signal (according to Eq. (1)), when either ionisation or spectral diffusion is dominant (setting $\gamma_r \approx 0$). **c** No significant spectral diffusion or ionisation is observed when the lasers are turned off. The solid line is a fit to the data using Eq. (1). Dashed grey line denotes the set threshold (in a 2 ms window). **d** Experiment and fit under 20 nW of NIR laser power (916 nm). **e** Experiment and fit under 1 μW of repump laser power. **f** Extracted saturation-diffusion rates, obtained at laser powers of ~20 nW (resonant) and ~5 μW (repump). See supplementary Fig. 3 for underlying data and error analysis.

lasers (20 nW, Fig. 3d), and (iii) illumination with the repump laser (1 μW, Fig. 3e). We observe a wide range of dynamics, from the microsecond to second timescale, and observe excellent agreement between the data and the model (solid lines are fits to Eq. (1)).

To quantitatively extract ionisation and diffusion rates under the perturbations, we set $\Gamma = 36$ MHz, (independently determined in Fig. 4e). We find that extracted rates are weakly dependent on the set threshold value, resulting from non-perfect initialisation on-resonance, but converge for higher T (Supplementary note 2). Averaging over a range of threshold values, we find diffusion rates $\gamma_d = 0.00(2)$ GHz s^{-1}, $0.60(2)$ GHz s^{-1}, $2.4(2) \times 10^3$ GHz s^{-1}, for perturbations (i), (ii) and (iii), respectively. Note that for larger Γ (e.g. at elevated temperatures[36]), the relative contribution of slow spectral diffusion decreases and the measurement uncertainty for γ_d increases. In the dark, where almost no diffusion is apparent, the fit only converges if we set $\gamma_i, \gamma_r = 0$, which is a reasonable assumption at 4 K, given the deep-level nature of the V2 centre[17,35].

Ionisation effects are only observed under the NIR-laser perturbation, due to the short diffusion timescale during the repump-laser perturbation (resulting in divergent fit results for γ_i and γ_r). From the data in Fig. 3d, we extract $\gamma_i = 1.0(2)$ Hz and $\gamma_r = 0.03(4)$ Hz. Correcting for reduced ionisation when the V2 centre is off-resonance with the NIR lasers results in an ionisation rate $\gamma_i^0 = 3(1)$ Hz (see Supplementary note 1).

We repeat the experiments for various laser powers, and observe a saturation-type behaviour of the diffusion rates, both under NIR-lasers and repump laser excitation (Supplementary Fig. 3). The higher saturation-diffusion rate measured for the repump laser is likely due to the larger fraction of charge traps that can be ionised via a single-photon process (see Figs. 1b and 3f). Different V2 centres in the material, show some variation in the (saturation) diffusion rates (Supplementary Figs. 4 and 8). Note that the behaviour at powers beyond those accessed in these experiments will determine if spectral stability persists under repeated fast optical π-pulses, as commonly used for remote entanglement generation experiments[7,14,18].

Check-probe spectroscopy: linewidth

Having established the spectral diffusion timescales, we characterise the homogeneous linewidth. We use an optical spectroscopy method that leverages the high-bandwidth nature of the check-probe scheme (similar to ref. 40) to mitigate linewidth broadening due to spectral diffusion. This is in contrast with conventional 'scanning PLE', which averages over diffusion dynamics faster than the acquisition timescale needed to obtain sufficient data over the full scanning frequency range[10,13,15,16,19,41] (typically ~s timescale, Supplementary Fig. 8. This is especially relevant for systems that are sensitive to laser-induced diffusion (such as the one considered here) for which the

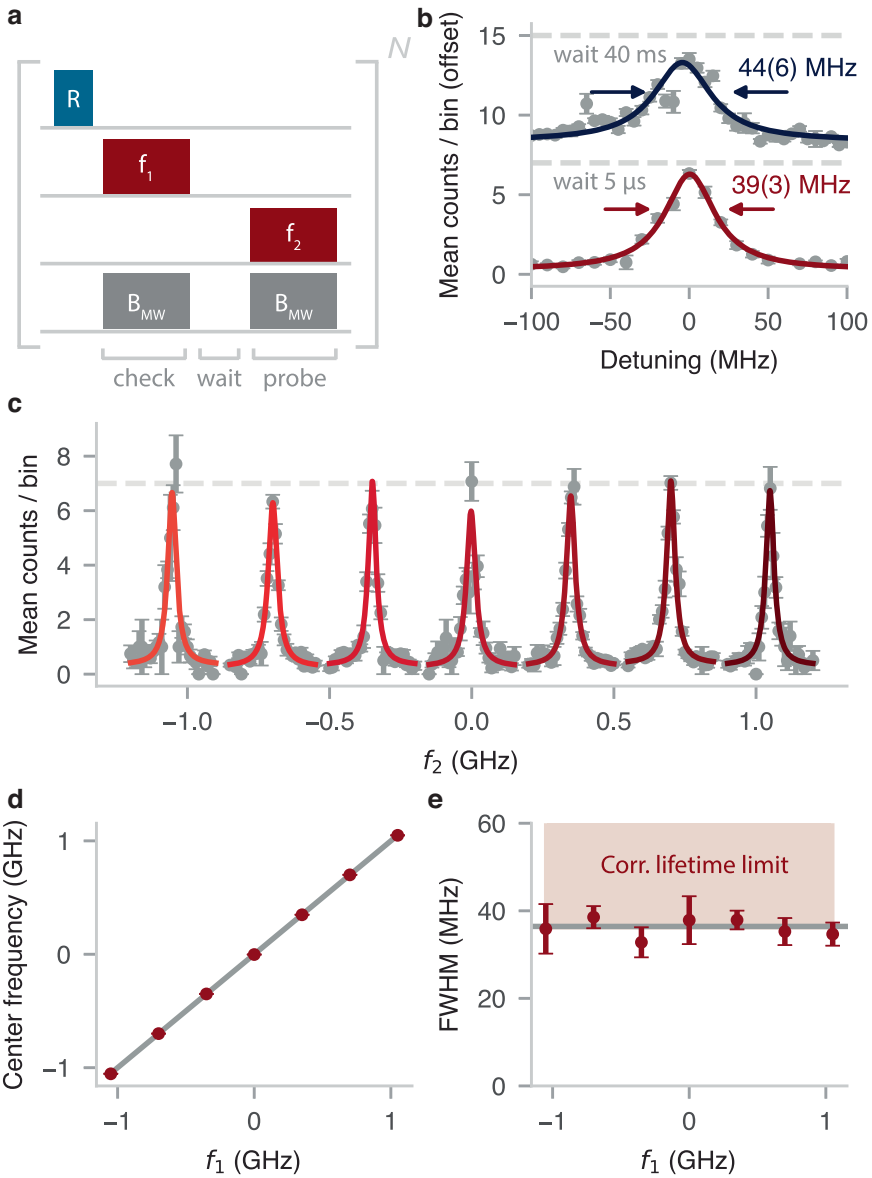

Fig. 4 | Homogeneous linewidth and state preparation. a Experimental sequence. A resonant laser at f_1 and a microwave (MW) pulse resonant with the ground-state spin transition act as a resonance check, initialising the optical transition near f_1. Next, a second laser probes the defect emission at f_2 (for 2 ms), yielding a measurement of the linewidth with minimal disturbance. **b** Experimental data showing narrow optical transitions, with the bottom (top) data corresponding to a waiting time of 5 μs (40 ms) between the f_1 and f_2 laser pulses (offset for clarity). Data are fitted to a Lorentzian with a FWHM of 39(3) MHz (44(6) MHz). The counts threshold is set to $T = 7$ during the f_1 pulse. **c** Data and fits as in (**b**) (bottom), scanning f_2 around f_1, when f_1 is set at different frequencies (various shades of red) within the broad diffusion-averaged line measured in Fig. 1g. **d** Measured resonance center frequency as a function of the set f_1 frequency (solid grey line: $f = f_1$). The defect emission frequency can effectively be tuned over a GHz range. **e** Corresponding linewidths extracted from (**c**), with inverse-variance weighted mean 36(1) MHz (solid grey line). The shaded region denotes the expected minimum linewidth (~36 MHz), given the lifetime limit of ~20 MHz, and correcting for power broadening (~26 MHz, Fig. 5j) and residual inhomogeneous broadening (~15 MHz, Eq. (2)).

check-probe scheme only requires laser illumination on timescales short compared to the laser-induced diffusion timescales.

First, we execute an alternative implementation of the 'check' block (compared to Figs. 2a and 3a), that consists of a single NIR-laser pulse at f_1, together with an MW pulse that mixes the spin states (Fig. 4a). By post-selecting on high counts, either the A_1 or A_2 transition is initialised on-resonance with f_1. A second laser is used to probe the defect emission at a frequency f_2 immediately thereafter (~μs timescale, here limited by the microprocessor clock cycle). By studying the mean number of counts during the f_2 pulse, (an upper bound for) the homogeneous linewidth can be extracted (Fig. 4b).

We introduce a quantitative model for the signal that extracts the homogeneous linewidth and considers the residual inhomogeneous broadening resulting from non-perfect initialisation on-resonance. To this end, we compute the spectral probability density immediately after the 'check' block, as a function of the number of detected photons $m \geq T$ using Bayesian inference (see Supplementary note 4):

$$P(f \mid m \geq T) = \frac{1}{N_T}\left(1 - \Gamma_i\left[T, \lambda(f - f_1)\right]\right), \tag{2}$$

with f the emitter frequency, $\lambda(f)$ the pure (i.e. homogeneous) spectral response of the emitter, $\Gamma_i[a, z]$ the incomplete Gamma function and N_T a normalisation constant (Supplementary note 4). The expression in Eq. (2) is strongly dependent on T, with higher threshold values leading to distributions that are sharply peaked around f_1. Note that this analysis assumes negligible laser-induced diffusion during the 'check' block, placing limits on the used laser power and the block's duration ($\ll 1/\gamma_d$).

The measured signal, i.e. the mean number of detected counts in the 'probe' block is then given by:

$$C(f) = P(f \mid m \geq T) * \lambda(f), \tag{3}$$

where $*$ denotes the linear convolution. Importantly, as both terms in Eq. (3) contain $\lambda(f)$, the pure spectral response can be recovered by varying T in post-processing (Supplementary note 4). In particular, for the Lorentzian spectral response:

$$\lambda_L(f) = C_0 \frac{\left(\frac{\Gamma}{2}\right)^2}{f^2 + \left(\frac{\Gamma}{2}\right)^2}, \tag{4}$$

with FWHM Γ and on-resonance brightness C_0, the signal converges to: $C(f) \to \lambda_L(f - f_1)$ at high threshold values ($T \gg \max[\lambda(f)]$), simplifying the analysis (Supplementary note 4).

We demonstrate the check-probe spectroscopy method on the same V2 centre as used in Figs. 1f, 2 and 3 (Methods), and observe narrow Lorentzian resonances around the f_1 laser frequency (39(3) MHz at $T = 7$, see Fig. 4b). Correcting for residual broadening by fitting Eq. (3) to the data for $1 \le T \le 13$ (using Eqs. (2) and (4)), we extract: $C_0 = 6.5(1)$ counts (3.22(7) kHz count rate) and Γ = 33(1) MHz. This spectrum (as well as the those measured in Fig. 5) corresponds to an average over the A_1 and A_2 transitions, resulting in: $\Gamma \approx (\Gamma_{A_1} + \Gamma_{A_2})/2$ (<5% deviation, assuming equal initialisation probability, see Supplementary note 5). Note that this ambiguity between the transitions can be fully resolved by executing the 'check' block with two NIR lasers, as in Fig. 2. The discrepancy between the extracted mean linewidth and the mean lifetime limit (~20 MHz) is well-explained by power-broadening, with optical Rabi frequencies estimated to be ~26 MHz (next section, see Fig. 5j).

Next, to verify our previous inference that spectral diffusion is virtually absent without laser illumination (Fig. 3c), we insert a 40 ms waiting time between the f_1 and f_2 pulses (Fig. 4b, top), which does not increase the linewidth within the fit error ($T = 7$). Importantly, this allows for the preparation of the transition at a specific frequency, 'storing' it in the dark, so that the V2 centre can be used to produce coherent photons at a later time. Furthermore, the broad nature of the diffusion-averaged linewidth depicted in Fig. 1f, enables probabilistic tuning of the emission frequency over more than a gigahertz[18]. We demonstrate this by varying the f_1 frequency, initialising the emitter at different spectral locations, and probing the transition with the NIR laser at frequency f_2 (Fig. 4c–e). Such tuning of the V2 emission frequency without the need for externally applied electric fields[31,32] might open up new opportunities for optically interfacing multiple centres.

Landau-Zener-Stückelberg interference

To further benchmark the check-probe spectroscopy method, we use it to resolve Landau-Zener-Stückelberg (LZS) interference fringes in the optical spectrum[25]. Such fringes demonstrate coherent control of the orbital states of the V2 defect using MW frequency electric fields, and enable the independent determination of the optical coherence and Rabi frequency[25], allowing for the separation of their contributions to the linewidths measured in Fig. 4.

LZS interference fringes can arise when a strong AC electric field shifts the optical transition across the laser frequency multiple times within the coherence time of the emitter[32,42]. Each time a crossing occurs, the emitter is excited with a small probability amplitude and associated 'Stückelberg' phase. These amplitudes can interfere constructively or destructively, creating fringes in the spectrum (see ref. 25 for an extensive review on the phenomenon).

In our setup, MW radiation is applied by running an AC current through an aluminium alloy wire spanned across the sample (Fig. 5a). The original purpose of the wire is to enable mixing of the ground-state spin in the 'check' and 'probe' blocks used in Fig. 4. However, this geometry also creates significant electric fields at microwave frequencies (Fig. 5a). Taking the defect ground and excited states as basis states ($|g\rangle = |0\rangle$ and $|e\rangle = |1\rangle$), the (optical) evolution of the system is described by the Hamiltonian (in the rotating frame of the emitter)[42]:

$$H = \frac{\Omega}{2}\sigma_x + \frac{\delta + A\cos(\omega t)}{2}\sigma_z, \tag{5}$$

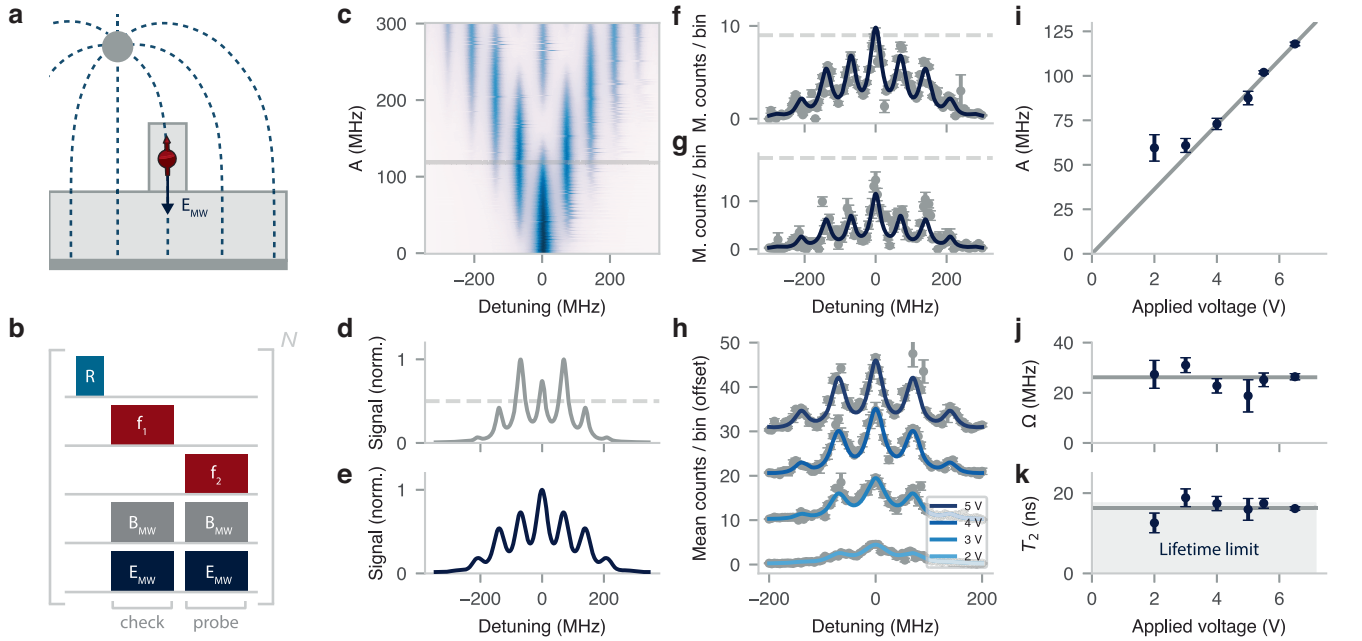

Fig. 5 | Landau-Zener-Stückelberg (LZS) interference. a Schematic showing the electric-field generated by the MW drive, connecting the bond wire and ground plane (dark grey, not drawn to scale), which can generate significant stark shifts. **b** Sequence, as in Fig. 4a, but now explicitly including the electric field (E_{MW}). **c** Characteristic LZS interference pattern (theory) as function of the laser detuning, and the electric field strength A. At higher electric fields, side bands emerge at multiples of the driving frequency $\omega = 70$ MHz. **d** Line cut through (c) for $A = 118$ MHz. The dashed line denotes an example threshold T. **e** The experimental spectrum expected from the situation in (d). The signal differs from the original spectrum as it is weighted over the probability to pass the threshold for different detuning. **f** Mean detected counts as a function of the two-laser detuning when the MW amplitude is set to 6.5 V, approximately equal to the value in (d). The threshold ($T = 10$) is set to about half the maximum amplitude, as in (d). The fit function (solid line) is obtained by fitting the dataset for a range of threshold values (see Supplementary Fig. 6). **g** Same dataset as in (**f**), but with $T = 20$. The signal distortion due to the threshold is well-captured by the fit. **h** Experimental data (grey) and fit (solid lines) as in (**f**), varying the applied voltage ($T = \{6, 10, 13, 15\}$). Data are offset by 10 counts for clarity. **i** Extracted electric field strength A as a function of the applied voltage. The solid grey line is a linear guide to the eye. **j** Extracted optical Rabi frequency Ω. Solid grey line denotes the inverse-variance weighted mean. **k** Extracted optical coherence time T_2. The shaded region denotes the mean lifetime limit: $T_2 = 2T_1 \approx 17$ ns. Solid grey line denotes the inverse-variance weighted mean of the data points.

where Ω is the optical Rabi frequency, δ is the detuning between the optical transition and the laser frequency, A is the stark-shift amplitude (which scales with the electric field amplitude), ω is the MW driving frequency and σ_x, σ_z are the Pauli spin matrices. For the experimental parameters used here, the system is considered to be in the 'fast-passage' regime (defined as $A\,\omega \gg \Omega^2$[25]), meaning the excitation probability amplitude during a single crossing is small (Methods). In this regime, the spectral response of the emitter can be described by[25]:

$$\lambda_{\mathrm{LZS}}(f) = C_0 \sum_k \frac{\Omega_k^2}{\frac{1}{T_1 T_2} + \frac{T_2}{T_1}\left(k\omega - f\right)^2 + \Omega_k^2}, \tag{6}$$

where C_0 is the on-resonance emitter brightness for $A = 0$, $\Omega_k = \Omega J_k\left(\frac{A}{\omega}\right)$, with J_k the Bessel function, and T_1, T_2 are the emitter's optical relaxation and (pure-dephasing) coherence times respectively. Figure 5c shows the optical spectrum as a function of A, obtained by evaluating Eq. (6) for our sample parameters. At higher electric field amplitudes (i.e. higher A), multiple characteristic interference fringes appear, spaced by the driving frequency ω (here 70 MHz), creating a complex optical spectrum.

Measuring such complex spectra with the check-probe optical spectroscopy method requires taking into account signal distortions arising from the form of the spectral probability density after the check block (Eq. (2)). To see why this is the case, we consider an exemplary theoretical spectrum plotted in Fig. 5d (for $A = 118$ MHz), where the threshold T is set to about half the maximum signal amplitude (dashed line in Fig. 5d). Such a threshold is passed (with high probability) not only when the central peak is on resonance with f_1, but also when one of the nearest fringes is on resonance with the laser. Computing the resulting weighted signal (inserting Eq. (6) in Eq. (3)) yields the distorted, experimentally expected spectrum shown in Fig. 5e.

To experimentally measure the LZS interference signal, we execute the sequence in Fig. 5b, now explicitly including the electric field components generated by the MW drive. These components were also implicitly present in previously discussed experiments (Fig. 4), but their effects could largely be neglected under the conditions: $\omega > A$ and $\omega > \Gamma \approx \sqrt{(\pi T_2)^{-2} + \Omega^2}$[25]. We set the MW driving frequency ω to the ground-state zero field splitting (70 MHz), so that the magnetic field components efficiently mix the spin states[19,43], and set the (peak-to-peak) MW amplitude between the wire and the ground plane to 6.5 V. Figure 5f and g show the measured spectrum for a threshold of $T = 10$ and $T = 20$ respectively. The former corresponds roughly to the example threshold in Fig. 5d, and the observed signal matches well with the expected spectrum in Fig. 5e. Setting $T = 20$ alters the measured spectrum, highlighting the interplay between the threshold and corresponding distortion. The solid lines are generated by a single fit of the complete dataset using Eq. (3) for $1 < T < 21$ (post-processed, see Supplementary Fig. 6).

We repeat this procedure while varying the MW amplitude (Fig. 5h) and extract A, Ω and the estimated pure-dephasing T_2 coherence time (Fig. 5i, j and k), keeping ω and the optical relaxation time $T_1 = 8.7$ ns fixed (again using the mean of the A_1 and A_2 transitions[26]). For amplitude values above 2 V we observe a linear relation between the MW amplitude and A, as expected. For lower values, a significant deviation is observed, possibly because the system is no longer well-described by the fast-passage limit (i.e. $A\,\omega \sim \Omega^2$). Indeed, the optical Rabi frequency is estimated to be 26(1) MHz (weighted mean of Fig. 5j), on the order of $\sqrt{A\,\omega}$. Finally, we find a mean $T_2 = 16.4(4)$ ns, approximately equal to the mean lifetime limit ($2\,T_1 \approx 17$ ns[26]).

Discussion

In this work, we introduced a high-bandwidth check-probe scheme that allows for quantitative characterisation of spectral diffusion and ionisation processes under the influence of external perturbations. Our methods enable measurements of the homogeneous transition linewidth of single quantum emitters, under minimal system disturbance.

We applied these methods to study the optical coherence of the V2 centre in commercially available bulk-grown silicon carbide. Despite high levels of spectral diffusion under laser illumination, we reveal near-lifetime-limited linewidths with slow dynamics, enabling the preparation of a frequency-tunable coherent optical transition[18,31,32]. Although higher purity materials are likely desired, such coherent optical transitions in bulk-grown SiC might enable nanophotonic device development, testing and characterisation (e.g. cavity coupling, Purcell enhancement) using widely available materials[44]. Studying defects integrated in nanocavities is of special interest, as their proximity to surfaces can significantly alter spectral diffusion dynamics. Future avenues for research in bulk-grown material include investigating the spin coherence properties and the spectral stability under higher-power laser pulses used for long-distance entanglement generation[7,8].

Finally, the presented methods are applicable to other platforms where spectral diffusion forms a natural challenge, such as rare-earth-doped crystals[45], localised excitons[30] or semiconductor quantum dots[29], and might enable new insights in the charge environment dynamics of such systems.

Methods

Sample parameters

The sample was diced directly from a 4-inch High-Purity Semi-Insulating (HPSI) wafer obtained from the company Wolfspeed, model type W4TRF0R-0200. We note that the HPSI terminology originates from the silicon carbide electronics industry. In the quantum technology context considered here, this material has a significant amount of residual impurities (order ~10^{15} cm^{-3} according to Son et al.[35]) and is hence considered low purity with respect to a concentration of ~10^{13} cm^{-3} typical for epitaxially grown layers on the c-axis of silicon carbide[15,46]. On a different sample, diced from a wafer with the same model type, a Secondary-Ion Mass Spectroscopy (SIMS) measurement determined the concentration of nitrogen donors as [N] = 1.1×10^{15} cm^{-3}. In addition to intrinsic silicon vacancies, we generate additional silicon vacancies through a 2 MeV electron irradiation with a fluence of 5×10^{13} cm^{-2}. The sample was annealed at 600 °C for 30 min in an Argon atmosphere. To enhance the optical collection efficiency and mitigate the unfavourable V2 dipole orientation for confocal access along the SiC growth axis (c-axis), we fabricate nanopillars. We deposit 25 nm of Al_2O_3 and 75 nm of nickel on lithographically defined discs. A subsequent SF_6/O_2 ICP-RIE etches the pillars, see figure 1c. The nanopillars have a diameter of 450 nm at the top and 650 nm at the bottom and are 1.2 μm high. We note that, considering the modest efficiency of our detector (≈25% at 950 nm), photon detection rates from the single V2 centres studied here (~15 kHz, see Fig. 2c) - while consistent with other reports on HPSI[22] - appear to be high compared to recently reported values on epitaxially grown layers[19,41,43,47]. This discrepancy might indicate that the photo-physics, including the metastable state dynamics, depend on the material purity, but this has not been further investigated in this work.

Experimental setup

All experiments are performed using a home-built confocal microscopy setup at 4K (Montana Instruments S100). The NIR lasers (Toptica DL Pro and the Spectra-Physics Velocity TLB-6718-P) are frequency-locked to a wavemeter (HF-Angstrom WS/U-10U) and their power is modulated by acousto-optic-modulators (G&H SF05958). A wavelength division multiplexer (OZ Optics) combines the 785 nm repump (Cobolt 06-MLD785) and NIR laser light, after which it is focused onto the sample by a movable, room temperature objective (Olympus MPLFLN 100x), which is kept at vacuum and is thermally isolated by a heat shield. A 90:10 beam splitter that directs the laser light into the objective, allows V2 centre phonon-sideband emission to pass through, to be detected on an avalanche photodiode (COUNT-50N, filtered by a Semrock FF01-937/LP-25 long pass filter at a slight angle). Alternatively, emission can be directed to a spectrometer (Princeton Instruments IsoPlane 81), filtered by a 830 nm long pass filter (Semrock BLP01-830R-25). Microwave pulses are generated by an arbitrary-waveform generator (Zurich Instruments HDAWG8), amplified (Mini-

circuits LZY-22+), and delivered with a bond-wire drawn across the sample. The coarse time scheduling (1 μs resolution) of the experiments is managed by a microcontroller (ADwin Pro II). For a schematic of the setup see Supplementary Fig. 9.

Magnetic field

For the check-probe optical spectroscopy measurements in Fig. 4 and Supplementary Fig. 8, we apply an external magnetic field of ≈1 mT along the defect symmetry axis (c-axis). All other experiments are performed at approximately zero field. We apply the field by placing a permanent neodymium magnet outside the cryostat. We align it by performing the sequence depicted in Fig. 1e, with f_1 set at the centre frequency of the broad resonance (Fig. 1f), and monitoring the average photoluminescence (f_1 pulse is set to 2 ms). A (slightly) misaligned field causes spin-mixing between the $m_s = \pm\frac{3}{2}$ and $m_s = \pm\frac{1}{2}$ subspace, which increases the detected signal. Minimising for the photoluminescence thus optimises the field alignment along the symmetry axis.

LZS fast-passage regime

The fast-passage regime is defined by: $A\omega \gg \Omega^2$ [25], with $\omega = 70$ MHz. From the measurements in Fig. 4, we can estimate: $\Omega < 40$ MHz. Furthermore, we can get a rough estimate for A by approximating the electric field at the defect to be: $E \approx \frac{U}{d}(\epsilon + 2)/3$, with U the applied voltage, $d \approx 500\,\mu$m the distance between the wire and the ground plane and $\epsilon \approx 10$ the dielectric constant of silicon carbide (using the local field approximation[32]). There is some debate on the value of the Stark-shift coefficient[31,32]. Here, we take the value from ref. 32: 3.65 GHz m MV^{-1} and estimate $A \approx 29$ MHz for an applied voltage of 1 V. Hence, $A\omega > \Omega^2$ for $U > 1$ V, and the fast-passage requirement is satisfied for most measurements in Fig. 5. The excellent agreement between the data and our model (especially for higher values of U) and the corresponding extracted values for Ω and A, further justify using the fast-passage solution of the LZS Hamiltonian.

Error analysis

For all quoted experimental values, the value between brackets indicates one standard deviation or the standard error obtained from the fit (unless stated otherwise). The error bars on the mean counts are based on Poissonian shot noise. The uncertainty on fit parameters is rescaled to match the sample variance of the residuals after the fit.

Data availability

All data underlying the study are available on the open 4TU data server under accession code: https://doi.org/10.4121/9d3f41e9-ddcd-4153-8508-2a9a9d5ea654.v1.

Code availability

Code used to operate the experiments is available on request.

Received: 9 October 2024; Accepted: 6 February 2025;
Published online: 22 February 2025

References

1. Waldherr, G. et al. Quantum error correction in a solid-state hybrid spin register. *Nature* **506**, 204–207 (2014).
2. Cramer, J. et al. Repeated quantum error correction on a continuously encoded qubit by real-time feedback. *Nat. Commun.* **7**, 11526 (2016).
3. Abobeih, M. H. et al. Fault-tolerant operation of a logical qubit in a diamond quantum processor. *Nature* **606**, 884–889 (2022).
4. De Bone, S., Möller, P., Bradley, C. E., Taminiau, T. H. & Elkouss, D. Thresholds for the distributed surface code in the presence of memory decoherence. *AVS Quantum Sci.* **6**, 033801 (2024).
5. Pompili, M. et al. Experimental demonstration of entanglement delivery using a quantum network stack. *npj Quantum Inf.* **8**, 1–10 (2022).
6. Knaut, C. M. et al. Entanglement of nanophotonic quantum memory nodes in a telecom network. *Nature* **629**, 573–578 (2024).
7. Pompili, M. et al. Realization of a multinode quantum network of remote solid-state qubits. *Science* **372**, 259–264 (2021).
8. Hermans, S. L. N. et al. Qubit teleportation between non-neighbouring nodes in a quantum network. *Nature* **605**, 663–668 (2022).
9. Wolters, J., Sadzak, N., Schell, A. W., Schröder, T. & Benson, O. Measurement of the ultrafast spectral diffusion of the optical transition of nitrogen vacancy centers in nano-size diamond using correlation interferometry. *Phys. Rev. Lett.* **110**, 027401 (2013).
10. Orphal-Kobin, L. et al. Optically coherent nitrogen-vacancy defect centers in diamond nanostructures. *Phys. Rev. X* **13**, 011042 (2023).
11. Faraon, A., Santori, C., Huang, Z., Acosta, V. M. & Beausoleil, R. G. Coupling of nitrogen-vacancy centers to photonic crystal cavities in monocrystalline diamond. *Phys. Rev. Lett.* **109**, 033604 (2012).
12. Ruf, M. et al. Optically coherent nitrogen-vacancy centers in micrometer-thin etched diamond membranes. *Nano Lett.* **19**, 3987–3992 (2019).
13. Robledo, L., Bernien, H., Van Weperen, I. & Hanson, R. Control and coherence of the optical transition of single nitrogen vacancy centers in diamond. *Phys. Rev. Lett.* **105**, 177403 (2010).
14. Bernien, H. et al. Heralded entanglement between solid-state qubits separated by three metres. *Nature* **497**, 86–90 (2013).
15. Heiler, J. et al. Spectral stability of V2 centres in sub-micron 4H-SiC membranes. *npj Quantum Mater.* **9**, 34 (2024).
16. Koch, M. K., Bharadwaj, V. & Kubanek, A. Limits for coherent optical control of quantum emitters in layered materials. https://doi.org/10.48550/arXiv.2312.11090 (2023).
17. Candido, D. R. & Flatté, M. E. Suppression of the optical linewidth and spin decoherence of a quantum spin center in a p - n diode. *PRX Quantum* **2**, 040310 (2021).
18. Brevoord, J. M. et al. Heralded initialization of charge state and optical-transition frequency of diamond tin-vacancy centers. *Phys. Rev. Appl.* **21**, 054047 (2024).
19. Babin, C. et al. Fabrication and nanophotonic waveguide integration of silicon carbide colour centres with preserved spin-optical coherence. *Nat. Mater.* **21**, 67–73 (2022).
20. Lukin, D. M., Guidry, M. A. & Vučković, J. Integrated quantum photonics with silicon carbide: challenges and prospects. *PRX Quantum* **1**, 020102 (2020).
21. Hausmann, B. J. M. et al. Fabrication of diamond nanowires for quantum information processing applications. *Diam. Relat. Mater.* **19**, 621–629 (2010).
22. Radulaski, M. et al. Scalable quantum photonics with single color centers in silicon carbide. *Nano Lett.* **17**, 1782–1786 (2017).
23. MacQuarrie, E. R. et al. Generating T centres in photonic silicon-on-insulator material by ion implantation. *N. J. Phys.* **23**, 103008 (2021).
24. Anderson, C. P. et al. Electrical and optical control of single spins integrated in scalable semiconductor devices. *Science* **366**, 1225–1230 (2019).
25. Shevchenko, S., Ashhab, S. & Nori, F. Landau–Zener–Stückelberg interferometry. *Phys. Rep.* **492**, 1–30 (2010).
26. Liu, D. et al. The silicon vacancy centers in SiC: Determination of intrinsic spin dynamics for integrated quantum photonics. *npj Quantum Inf.* **10**, 72 (2024).
27. Fang, R.-Z. et al. Experimental generation of spin-photon entanglement in silicon carbide. *Phys. Rev. Lett.* **132**, 160801 (2024).
28. Higginbottom, D. B. et al. Optical observation of single spins in silicon. *Nature* **607**, 266–270 (2022).
29. Neuhauser, R. G., Shimizu, K. T., Woo, W. K., Empedocles, S. A. & Bawendi, M. G. Correlation between fluorescence intermittency and spectral diffusion in single semiconductor quantum dots. *Phys. Rev. Lett.* **85**, 3301–3304 (2000).

30. Iff, O. et al. Substrate engineering for high-quality emission of free and localized excitons from atomic monolayers in hybrid architectures. *Optica* **4**, 669 (2017).
31. Rühl, M., Bergmann, L., Krieger, M. & Weber, H. B. Stark tuning of the silicon vacancy in silicon carbide. *Nano Lett.* **20**, 658–663 (2020).
32. Lukin, D. M. et al. Spectrally reconfigurable quantum emitters enabled by optimized fast modulation. *npj Quantum Inf.* **6**, 1–9 (2020).
33. Pieplow, G. et al. Quantum Electrometer for time-resolved material science at the atomic lattice scale. https://doi.org/10.48550/arXiv.2401.14290 (2024).
34. Ji, W. et al. Correlated sensing with a solid-state quantum multisensor system for atomic-scale structural analysis. *Nat. Photon.* **18**, 230–235 (2024).
35. Son, N. T. & Ivanov, I. G. Charge state control of the silicon vacancy and divacancy in silicon carbide. *J. Appl. Phys.* **129**, 215702 (2021).
36. Udvarhelyi, P. et al. Vibronic states and their effect on the temperature and strain dependence of silicon-vacancy qubits in 4H-SiC. *Phys. Rev. Appl.* **13**, 054017 (2020).
37. Fleury, L., Zumbusch, A., Orrit, M., Brown, R. & Bernard, J. Spectral diffusion and individual two-level systems probed by fluorescence of single terrylene molecules in a polyethylene matrix. *J. Lumin.* **56**, 15–28 (1993).
38. Basché, T. (ed.) *Single-Molecule Optical Detection, Imaging and Spectroscopy* (VCH, Weinheim, 1997).
39. Zumofen, G. & Klafter, J. Spectral random walk of a single molecule. *Chem. Phys. Lett.* **219**, 303–309 (1994).
40. Hermans, S. L. N. et al. Entangling remote qubits using the single-photon protocol: An in-depth theoretical and experimental study. *N. J. Phys.* **25**, 013011 (2023).
41. Lukin, D. M. et al. Two-emitter multimode cavity quantum electrodynamics in thin-film silicon carbide photonics. *Phys. Rev. X* **13**, 011005 (2023).
42. Miao, K. C. et al. Electrically driven optical interferometry with spins in silicon carbide. *Sci. Adv.* **5**, eaay0527 (2019).
43. Banks, H. B. et al. Resonant optical spin initialization and readout of single silicon vacancies in 4H-SiC. *Phys. Rev. Appl.* **11**, 024013 (2019).
44. Lukin, D. M. et al. 4H-silicon-carbide-on-insulator for integrated quantum and nonlinear photonics. *Nat. Photonics* **14**, 330–334 (2020).
45. Thiel, C., Böttger, T. & Cone, R. Rare-earth-doped materials for applications in quantum information storage and signal processing. *J. Lumin.* **131**, 353–361 (2011).
46. Nagy, R. et al. High-fidelity spin and optical control of single silicon-vacancy centres in silicon carbide. *Nat. Commun.* **10**, 1954 (2019).
47. Körber, J. et al. Fluorescence enhancement of single V2 centers in a 4H-SiC cavity antenna. *Nano Lett.* **24**, 9289–9295 (2024).

Acknowledgements

We thank Florian Kaiser and Michel Orrit for useful discussions relating to the spectral diffusion measurements. We thank Tien Son Nguyen, Michael Flatté and Denis Candido for input on the charge stability and charge dynamics. We thank Benjamin Pingault for his input on the design of the experimental setup and Daniel Bedialauneta Rodriguez for his input during project discussions. We thank Yanik Herrmann for feedback on the manuscript. We thank Nico Albert and Tim Hiep for designing and machining parts for the setup, Henri Ervasti, Pieter Botma and Ravi Budhrani for software support and development, Régis Méjard and Hitham Mahmoud Amin for optical and safety support, Siebe Visser, Vinod Narain and Erik van der Wiel for general technical support and Jason Mensigh, Olaf Benningshof and Jared Croese for cryogenic and vacuum engineering support. This research was supported by the Quantum Internet Alliance through the European Union's Horizon Europe programme grant agreement No. 101080128. This project has received funding from the European Research Council (ERC) under the European Union's Horizon 2020 research and innovation programme (grant agreement No. 852410). This work was supported by the Dutch National Growth Fund (NGF), as part of the Quantum Delta NL programme. This work is part of the research programme NWA-ORC with project number NWA.1160.18.208, which is (partly) financed by the Dutch Research Council (NWO). This project has received funding from the European Union's Horizon Europe research and innovation programme under grant agreement No 101135699.

Author contributions

G.L.v.d.S, L.J.F., S.J.H.L. and T.H.T. devised the experiments. G.L.v.d.S., L.J.F. and A.D. performed the experiments and collected the data. G.L.v.d.S., L.J.F. and S.J.H.L. prepared the experimental apparatus. G.L.v.d.S., L.J.F., S.J.H.L. and T.H.T. analysed the data. G.M.T. and T.W.d.J. designed and fabricated the sample. G.L.v.d.S., L.J.F., S.J.H.L. and T.H.T. wrote the manuscript with input from all authors. T.H.T. supervised the project.

Competing interests

The authors declare no competing interests.

Additional information

Supplementary information The online version contains supplementary material available at https://doi.org/10.1038/s41534-025-00985-3.

Correspondence and requests for materials should be addressed to T. H. Taminiau.